Article

Rheology improvement for silicon nitride and resin slurries for vat photopolymerization printing and sintering

Check for updates

Corson L. Cramer[1] ✉, Nadim S. Hmeidat[1], David J. Mitchell[2], Patrick L. Snarr[3], Ercan Cakmak[4], Steve E. Bullock[1], Trevor G. Aguirre[1], Marco C. Martinez[4] & Beth L. Armstrong[4]

This work presents the formulation, rheological characterization, and sintering of silicon nitride (Si_3N_4) slurries for vat photopolymerization (VPP) using digital light processing (DLP). Bimodal Si_3N_4 powder was dispersed into commercial photopolymer resin using two different dispersants with opposing effects on surface charge, resulting in varied slurry stability and flow behavior. Slurries were engineered to exhibit shear-thinning behavior suitable for VPP, and their flow properties were quantified using a power-law fluid model. The formulations achieved cure depths of approximately 40 μm and enabled printing of green bodies. Post-processing included thermal debinding and liquid-phase sintering, yielding primarily β-Si_3N_4 with a minor Y-Si-Al-O-N glass phase. The sintered parts reached ~85% of theoretical density and demonstrated a flexural strength of ~330 MPa. Microstructural analysis revealed closed porosity along with some defects related to powder agglomeration and interlayer adhesion. These findings provide insights into slurry formulation strategies for additive manufacturing of high-performance non-oxide ceramics.

Silicon nitride (Si_3N_4) is an important engineering ceramic material because of its high hardness, strength, and wear resistance[1]. Additionally, the high-temperature stability, oxidation resistance up to 1700 °C, and corrosion resistance are important for energy applications such as in gas turbines, turbomachinery, and aero engines[2–6]. It is also a very useful material in biomedical implants and electromagnetic applications[7–9]. Traditionally, Si_3N_4 has been made using near net shape techniques like injection molding, gelcasting, slip casting, and tape casting[10–13].

Although these methods can provide highly dense microstructure with excellent mechanical properties, the cost associated with molds, tooling, and machining can be burdensome, and the ability to rapidly change part geometry and provide high throughput can be improved. A literature review focused on advanced manufacturing technologies for Si_3N_4 ceramics was completed[12], and it was recommended that methods to help improve throughput and design flexibility is additive manufacturing (AM), and there are many reported research efforts to provide solutions for ceramics[14,15]. Since the design parameters for such ceramics is becoming more demanding for many applications including energy, defense and biomedical[16], AM of Si_3N_4 is becoming increasingly important[17].

Methods such as extrusion, binder jet 3D printing, and selective laser sintering/melting[18–28] have been utilized to AM Si_3N_4, but because of low resolution, poor surface finish, and issues of sinterability for these techniques, this research focused on slurry develop for vat photopolymerization (VPP) using digital light projection (DLP). A schematic illustration of the VPP process is shown in Fig. 1. VPP has the ability to create high resolution green preforms that can be debound and sintered into fine featured net shapes with high surface quality and geometric accuracy[29]. One drawback to VPP with silicon nitride is the high refractive index of the powder leading to attenuation of the light and ability to penetrate deep into the slurry. Since limited commercial solutions for non-oxide ceramics exist in VPP or stereolithography-based techniques, custom slurry development is often needed for VPP[30] including rheological characterization, increased solids loading, optimization of the resin, solvent, and dispersants constituents to allow for printable slurries due to curing depth/refractive index relationships. For example, the base resins must have ample monomers and

[1]Manufacuting Science Division, Oak Ridge National Laboratory, Oak Ridge, TN, USA. [2]Department of Materials Science and Engineering, Department of Mechanical and Aerospace Engineering, University of Central Florida, Orlando, FL, USA. [3]Nuclear Energy and Fuel Cycle Division, Oak Ridge National Laboratory, Oak Ridge, TN, USA. [4]Materials Science and Technology Division, Oak Ridge National Laboratory, Oak Ridge, TN, USA. ✉e-mail: cramercl@ornl.gov

Fig. 1 | Schematic Illustration of the VPP 3D printing process of a photocurable slurry.
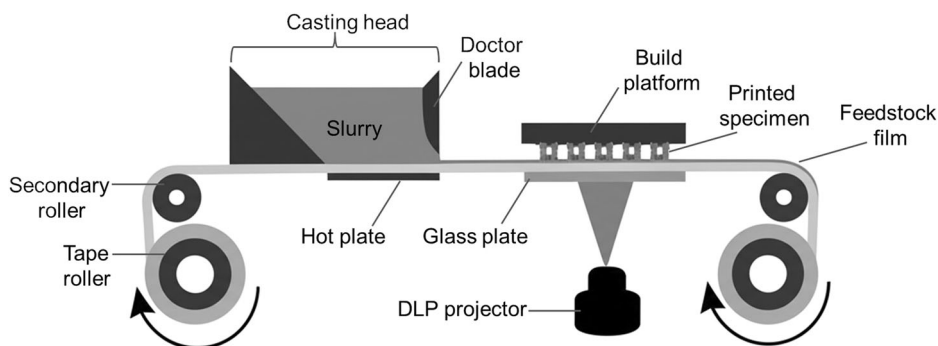
photoinitiator to cure, but the dispersants added must be compatible with the resin and effectively provide lower viscosity and shear-thinning behavior in the slurry.

Altun, et al. manufactured Si_3N_4 ceramic parts using the stereolithography-based ceramic manufacturing method with photopolymer-containing suspension[31], and Wu, et al. demonstrated suspensions with high-refractive index[32]. Huang et al. successfully made complex-shaped Si_3N_4 parts using surface-oxidized Si_3N_4 powder via DLP printing method[33]. Zhan et al. showed that VPP using SLA of Si_3N_4 is possible with variable light intensities and printing parameters[34]. Some of the most comprehensive studies where custom slurries were developed, printed, debound, and sintered with gas pressure are in the work of Schwarzer-Fischer et. al and pressureless sintering by Wang et al. and Chen et al., where both methods provide high density and high strength[35–37].

Li et al. highlighted the importance of rheology as a key parameter for the development of slurries for successful printing of silicon nitride[38]. Si_3N_4 slurries with high solids loading, low viscosity, and large cure depths were prepared and sintered to high density by adding silane couplers as dispersants, but unfortunately, those additives are expensive and difficult to incorporate in slurries[39–41]. Zou et al. formulated slurries from base constituents, not commercial resin, and could mix dispersants appropriately to obtain shear-thinning rheology[42]. Wu et al. utilized two commercial dispersants, CC42 and KD1, to formulate Si_3N_4 slurries with very stable suspension behavior with a slurry made from individual monomer constituents, and also obtained shear-thinning behavior[43]. However, it was not understood why both additives were needed and how they affected stability and rheology in the slurries.

In this study, two common dispersants seen in the literature were used to make UV-curable Si_3N_4 VPP slurries with a commercial ceramic resin from Admatec, and used DLP to better understand the dispersant mechanisms in VPP slurries utilizing dispersion characterization, shear-thinning rheological behavior, printability, and sinterability of Si_3N_4. The order of mixing while using two dispersants was tested to show the effects on rheology to obtain a printable slurry. The resulting shear-thinning behavior was quantified using a power-law fluid model, which enabled comparison against the rheological behavior of a commercial VPP slurry and facilitated the selection of the most suitable formulation for VPP printing.

Results

The size and morphology of the powder are important for the dispersion and sintering, so the particle size distribution of each powder was measured, as shown in Fig. 2. The distributions for the two sintering aid powders (alumina and yttria) were monomodal but different in size, where the D_{50} of the alumina was 0.728 μm and the D_{50} of the yttria was 23.18 μm. The distributions for both the E-03 and E-10 silicon nitride powders were bimodal, where the E-03 had some peaks higher than 100 μm and a prominent peak around 3 μm. The E-10 had some strong peaks around 70–80 μm and another one around 1 μm.

The distribution data from Fig. 2 can be seen in Table 1, where the $D_{10-50-90}$ and span are shown and calculated. The spans for the sintering aids
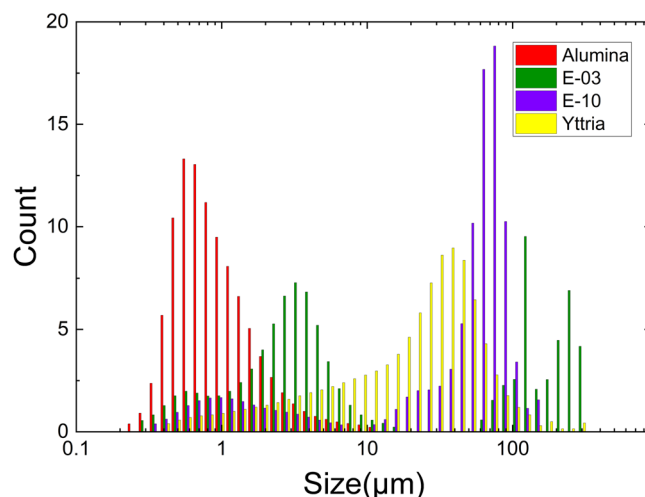

Fig. 2 | Particle size distribution in volume average for all powders.

Table 1 | Particle size distribution in volume average, surface area, and agglomeration data for all powders

	Alumina	Yttria	Si_3N_4 E-03	Si_3N_4 E-10
D_{10} (μm)	0.414	2.257	0.815	1.197
D_{50}	0.728	23.18	3.97	54.1
D_{90}	1.921	57.10	215	81.0
Span, $(D_{90}-D_{10})/D_{50}$	2.07	2.36	53.95	1.47
BET surface area, SA_{BET}, (m^2/g)	4.95	14.52	2.85	10.69
BET Particle size, D_{BET}, 6/ (SA_{BET}*density), (μm)	0.303	0.083	0.658	0.175
Agglomeration factor, D_{50}/D_{BET}	2.40	280.48	6.03	308.44

and the E-10 silicon nitride were in the 1–2 range, but the span for the E-03 silicon nitride was much higher around 54. BET surface area was also done to help understand the morphology and agglomeration. The surface area of the E-03 and E-10 silicon nitrides was very different, with the E-03 having a much lower surface area (2.85 m^2/g) compared to the E-10 (10.69 m^2/g). The yttria and alumina also had very different surface areas, where the alumina was around 5 m^2/g and the yttria was much higher of around 14.52 m^2/g. The particle size based on the BET estimate was also calculated for all the powders. Since the D_{50} was measured, the agglomeration factor can be determined, and from this calculation, the alumina and E-03 silicon nitride were not agglomerated (agglomeration factor < 10), but the yttria and the E-10 silicon nitride were highly agglomerated (agglomeration factor > 100).

Fig. 3 | SEM images of the powders used.
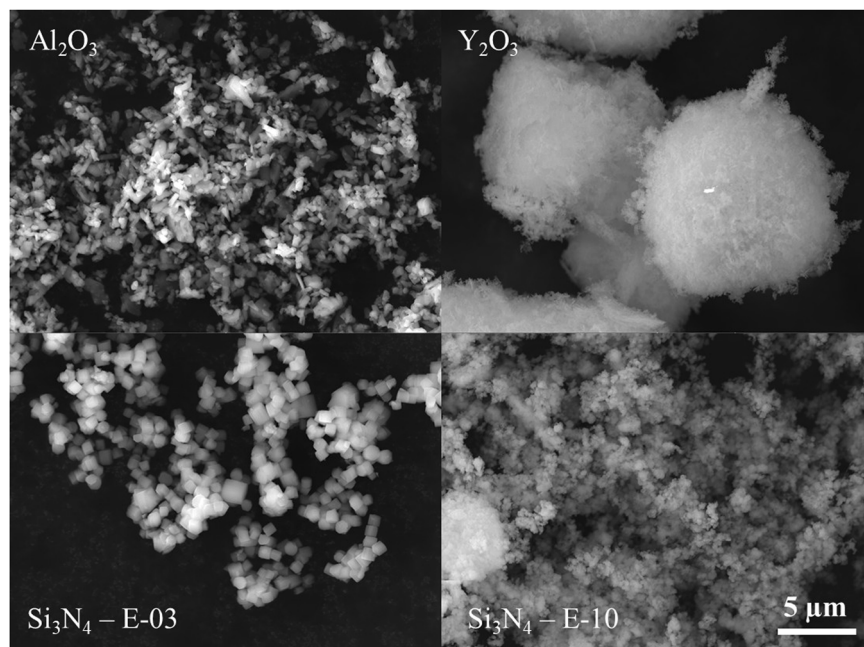
The morphology and size of all the powders are shown in the SEM images in Fig. 3. The alumina powder has mostly jagged and irregular shaped particles but seems to be well dispersed, which agrees with its low agglomeration factor of 2.40. In contrast, the yttria powder is agglomerated into particles around 10 μm, and this also agrees with its high agglomeration factor of 280.48. The E-03 Si_3N_4 powder has distinct cube-like shaped powder particles and do not seem to be bunch or agglomerated, and the agglomeration factor is low of 6.03. The E-10 Si_3N_4 powder shows very small particles with many areas of agglomerates smaller than 5 μm. Understanding the particle size, size ranges, morphology, and degree of agglomeration is important when developing slurries to better predict dispersant concentration and absorption needs, potential sedimentation during printing or aging of the slurries at rest, particle-particle interfaces, and their impact on sintering. The range of sizes presented in this paper may be challenging, but bimodal distributions of the base powder, which is silicon nitride here, have been known to disperse better in resins and provide higher cure depth[44,45]. The sizes of the powders, agglomerates, and the degree of agglomeration will also play a role in the defects that arise during processing after the printing is done.

Since previous literature suggested that both CC42 and KD1 provided the best dispersion, more data on how the surface charges interact with silicon nitride were investigated. As zeta potential is a useful tool in characterizing surface potential and resulting stability of powders in solvents, zeta potential was measured on each of the bare, untreated silicon nitride powders in toluene, as well as the silicon nitride powders with the additives to provide insight on the stability of the dispersants with the powders before making slurries. Toluene was used because it has a known refractive index. Zeta potential measurements in Table 2 indicate the stability for the two silicon nitride powders with and without the dispersants added at 2 wt.%. relative to the powder weight. The KD1 and the CC42 had opposite surface charges on both silicon nitride powders indicating that they have different ionic charges. On E03, CC42 was negatively charged (−66.23 mV) and KD1 was positively charged (34.91 mV) in toluene, and on E10, CC42 was −120.2 mV, and KD1 was 22.1 mV. The E-10 powder with CC42 was more stable shown in almost 2x higher zeta potential (−120.2 ± 20.4) versus the E-03 zeta potential (−66.23 ± 3.4). Since CC42 had higher absolute values of zeta potential on both the E-10 (|−120.2| mV) and E03 (|−66.23| mV) powder surfaces, it was theorized that it would provide better stability than KD1 when used in a slurry. Additionally, the KD1 is a solid and exhibited

Table 2 | Zeta potential measurements for dispersants used

	Dispersant	Dispersant concentration (wt.%)	Zeta potential (mV)	PSD (um)
E-10	No dispersant	--	13 ± 0.5	3.2 ± 0.7
	KD1	2	22.07 ± 3.5	2.6 ± 0.3
	CC 42	2	−120.2 ± 20.4	1.2 ± 0.4
E-03	No dispersant	--	6 ± 6.6	−20 ± 5.2
	KD1	2	34.91 ± 6.7	14.1 ± 3.7
	CC 42	2	−66.23 ± 3.4	4.9 ± 1.3

The aliquots were measured in toluene the day of mixing

solubility and mixing issues with resins; however, it does dissolve easily in toluene. The E-10 powder with KD1 was slightly more stable as shown in higher zeta potential with E-10 (34.91 ± 6.7) versus the E-03 zeta potential (22.07 ± 3.5); however, the difference is minimal as it is just outside the standard deviation of the measurement.

To fully understand the effectiveness of the dispersants' impact on slurry stability, rheological information is needed. Rheological characterization of slurries was conducted with these powders and dispersants, and the order of mixing was evaluated to provide insight to whether the dispersant materials exhibited competitive adsorption. The order of mixing of KD1 and CC42 was varied to produce slurries with low (<10 Pa·s at 10 s^{-1} shear rate) viscosity and shear-thinning behavior (provide slope or yield range to specify behavior) to accommodate the VPP printer requirements. As high solids (ideal ~50 vol.%, min >35 vol.%) for optimum densification control is needed, screening studies started at 35 vol.% with performing shear ramps rheological flow tests. Figure 4A shows data from the shear ramps in which slurries were made by adding KD1 as a solid before Si_3N_4 powder with CC42 added last (i.e. order of mixing: resin, KD1, E-03, E-10, CC42, yttria, alumina). Slurry 1KD1/4CC42 showed Newtonian behavior in the flow test. This signified that stability was reached when adding KD1 before the powder, and a total of 5 wt.% dispersant was used. However, the viscosity measured for this slurry system was higher than the desired printing viscosity range for the Admatec printer (~10 Pa·s at 10 s^{-1} shear rate). In addition, the preferred rheological behavior is shear-thinning
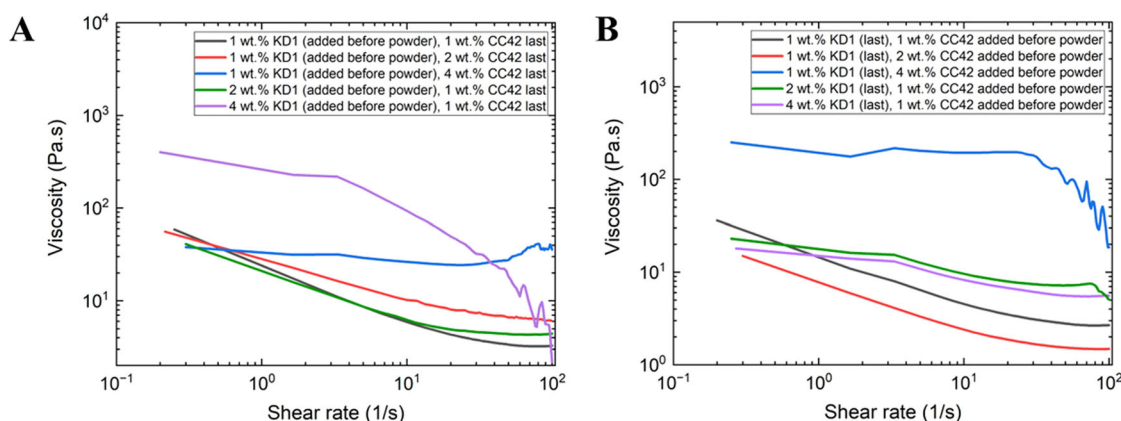
Fig. 4 | Initial rheology of slurries. Log-log plots of viscosity vs shear rate during the shear ramp flow tests for 35 vol.% slurries **A** in which KD1 was added before powder with CC42 added last, and **B** in which KD1 was added last with CC42 added before the powder.

because the slurry must not spread across the build plate until the doctor blade moves, flows, and spreads uniformly during printing, and then cease flow once printing is completed. As the CC42 content was decreased, the slurries began to exhibit shear-thinning behavior, and the viscosity decreased to the desired range of 10 Pa·s at 10 s^{-1} shear rate for slurry 1KD1/2CC42. Less CC42 means there is more surface area of the powder for KD1 to absorb, leading to stronger shear-thinning behavior. This trend is reflected in the power-law parameters, where the flow index (n) decreased from 0.89 to 0.55 and 0.37, and the consistency index (K) decreased from 33.8 to 28.1 and 24.3 Pa·s^n as CC42 loading was reduced from 4 to 2 and 1 wt.%, respectively (see Table S1 and Fig. S2). A similar trend occurred when the CC42 amount remained constant and the KD1 content increased, but likely there is extra dispersant that is not adsorbed in the slurry with high amount of dispersant like 1KD1/4CC42 and 4KD1/1CC42 (although adsorption tests were not done). Also, no aging tests or extra time for the first dispersant to absorb was given. Near-Newtonian behavior was also observed in the 4KD1/1CC42 slurry ($n = 0.77$, $K = 272.7$ Pa·s^n) within the shear rate range of 0.2–3 s^{-1}. As the KD1 content decreased, the slurries again became shear-thinning, and viscosity decreased to 7 Pa·s at 10 s^{-1} shear rate for slurry 2KD1/1CC42. This shows that when adding KD1 before powder, 1 wt.% provides more shear-thinning behavior ($n = 0.37$). When the total amount of dispersant was 5 wt.%, near-Newtonian behavior occurred ($n = 0.89$ for 1KD1/4CC42 and $n = 0.77$ for 4KD1/1CC42) (see Table S1 and Fig. S2).

Figure 4B shows slurries where KD1 was added as a solid last with CC42 added before the bimodal Si$_3$N$_4$ powders (i.e. order of mixing: resin, CC42, E-03, E-10, KD1, yttria, alumina). Slurry 4CC42/1KD1 showed Newtonian behavior in the flow test ($n = 0.87$; see Table S1 and Fig. S2). By decreasing the CC42 amount, again, the slurries became more shear-thinning ($n = 0.47$, 0.47, and 0.94 for CC42 loadings of 1, 2 and 4 wt.%, respectively) like the slurries in which KD1 was added first, but the minimum viscosity reached was for slurry 2CC42/1KD1 ($K = 7.85$ Pa·s^n) (see Table S1 and Fig. S2). This implies that there is an optimum amount to provide the lowest viscosity, which could mean that there was maximum absorption of CC42 at 2 wt.%. By varying the KD1 content with constant 1 wt.% CC42, the behavior of all three slurries is roughly the same with shear-thinning behavior and a viscosity of around 7–8 Pa·s at 10 s^{-1} shear rate ($K = 15.02$, 18.19, and 15.12 Pa·s^n for KD1 loadings of 1, 2, and 4 wt.%, respectively) (see Table S1 and Fig. S2). This means the KD1 was not providing stability when added last relative to the CC42. This also implies some competitive absorption where the CC42 could dominate surface charges even when added after the powder is mixed with KD1, and this may be from the much higher absolute value of zeta potential in CC42 from the amine groups and Cl$^-$ anions (KD1 likely only has methyl, hydroxyl, and carbonyl groups to interact with silicon nitride). For the printing process, the amount of 1–2 wt.% of either dispersant, mixed either way, provides the correct rheology.
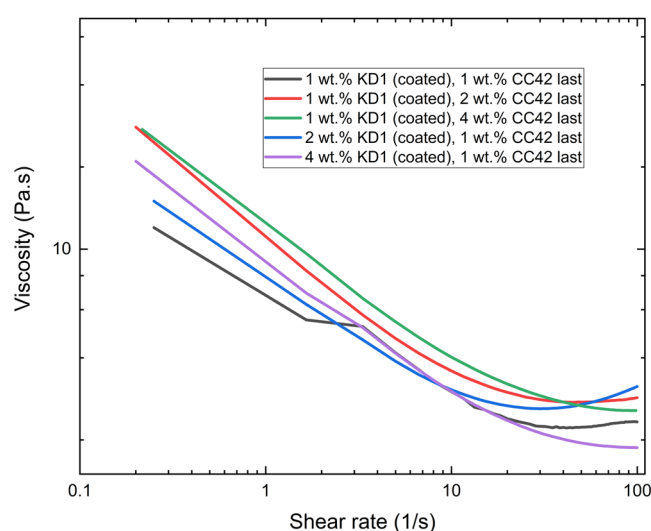

Fig. 5 | Shear ramp flow tests for 35 vol.% slurries in which KD1 was coated onto powder before adding to slurries in which CC42 was added last.

Since KD1 is a solid and can be difficult to incorporate into slurries that do not have a solvent, and because it was previous learned in Fig. 4 that CC42 is still affective when added last, or after silicon nitride powder, studies were conducted to coat or graft the Si$_3$N$_4$ powder with KD1 using a toluene sonication method before adding them into slurries[39,46].

Figure 5 shows the shear ramp results of slurries with 35 vol.% solids using Si$_3$N$_4$ powder (both E03 and E10 together) that was coated with KD1 before adding to slurries in which the CC42 was added last. This is very different behavior compared to the previous order of mixing plot in Fig. 4. All the slurries were shear-thinning with n values ranging between 0.3 and 0.64 (Fig. S3 and Table S1), but have lower viscosities (6–7 Pa·s at 10 s^{-1} shear rate) compared to the order of mixing results. Newtonian behavior was not observed this time. This could be due to strong absorption of KD1 with the coating method providing a better steric hindrance layer so that CC42 has less effect when slurries are made with the KD1-coated powder providing shear-thinning behavior regardless of the KD1 and CC42 amount.

Since the slurries made with coated KD1 powder had the requisite rheological behavior needed for printing, further characterization of the flow behavior of these slurries was performed at 40 vol.% solids, which is more characteristic of slurries that would be utilized, specifically to minimize the binder burnout duration and facilitate sintering to higher final densities. The viscosity of the slurries loaded to 40 vol.% was only 3–5 Pa·s higher relative to the same slurries with 35 vol.% (Fig. 6A); however, slurries
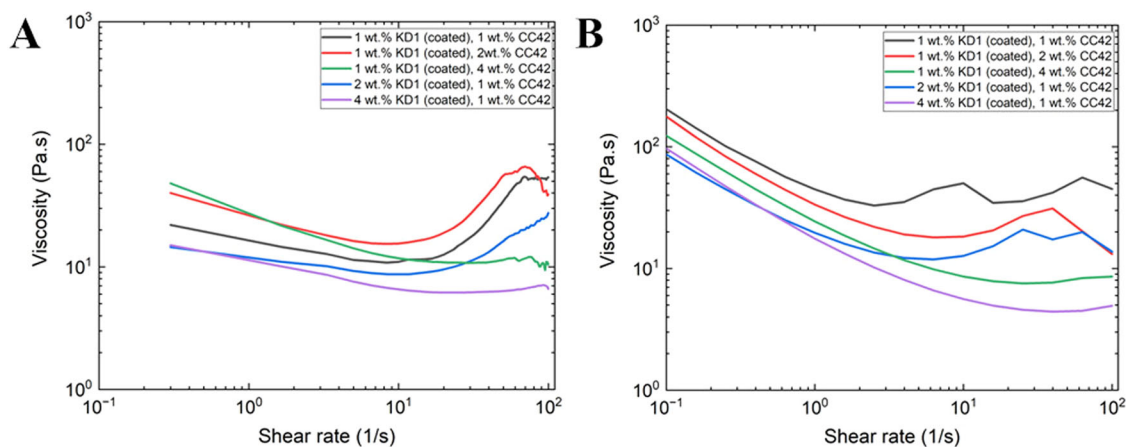
Fig. 6 | Rheology of 40 vol.% slurries with KD1 as a coating. Log-log plots of viscosity vs shear rate during the rheology flow tests for 40 vol.% slurries in which KD1 was coated onto powder before making slurries with CC42 added last for **A** short shear ramps and **B** longer shear sweeps.

like C1KD1/1CC42 and C1KD1/2CC42) exhibited shear-thickening behavior at shear rates of $10\,s^{-1}$ and higher. This also shows that more dispersant, either C1KD1/4CC42 or C4KD1/1CC42, helped return the shear-thickening behavior to almost Newtonian or partially shear-thinning behavior. The shear-thickening here was not permanent but worth studying further to find a time frame to ensure agglomeration and deagglomeration defects are not captured into the curing of layers. Shear-thickening behavior can cause issues when spreading the slurry onto transport foil or during the printing when the build plate presses into the slurry. The initial shear ramp studies were conducted over shear rates of 0.1 to $100\,s^{-1}$ in 2 min; thus, additional shear sweeps were conducted on these slurries to address concerns regarding the effect of shear rate ramp (Fig. 6B). The results indicate that the slurries exhibited stronger shear-thinning behavior during longer shear ramps, with *n* values ranging from 0.26 to 0.35, compared to 0.56 to 0.85 during short shear ramps. Additionally, the longer ramps reduced the extent of shear-thickening behavior over the $0.1–70\,s^{-1}$ shear rate range—for example, viscosity increased from 20 Pa·s to 70 Pa·s during short ramps but only to ~30 Pa·s during longer ramps in the C1KD1/2CC42 slurry at 40 vol.% (see Fig. S4 and Table S2). The two slurries selected for printing—both exhibiting strong shear-thinning behavior and viscosities below 10 Pa·s at $10\,s^{-1}$—were: (1) C1KD1/4C42 and (2) C4KD1/1CC42.

This is important moving forward into printing because the critical shear rate for shear-thickening behavior was $4–11\,s^{-1}$ as shown in Fig. 6B, and the slurries experienced two shear rate events before printing: (1) spreading under the doctor blade as the slurry exited the vat and (2) the pushing of the build plate into the slurry each time a slurry layer is cured during the printing. Each shear event has a different rate and effect on rheology.

The first shear event was the spreading of the slurry as it exited the vat. The shear rate experienced by spreading under the doctor blade during the transport of slurry during printing was $571\,s^{-1}$ (foil transport speed ÷ doctor blade height). This spreading shear rate of $571\,s^{-1}$ was beyond the shear-thickening zone for almost all slurries, but the slurries travel some distance before reaching the build plate area, so they have time to settle back to their original rheology before they reach the area where the build plate dips down into the slurry to commence printing. This time can be estimated (transport distance before printing ÷ transport speed + programmed time delay of 10 s + down transport distance ÷ distance from build plate to printing surface = 100,000 µm ÷ 40,000 µm/s + 10 s + 6000 µm ÷ 6,000 µm/s = 13.5 s). Since this first critical shear-thickening range of the slurries was exceeded by the shear rate experienced under the doctor blade, it may be a processing step where discontinuities occur, and is an area of further investigation.

Once the slurry is transported to the area right under the build plate, they experienced the second shear event, and this shear rate is produced by the build plate dipping down and pushing into the slurry. Assuming the 70 µm film from the doctor blade used in this study remained at that height

as it reached the printing area, then the shear rate experienced by pushing the build plate into the slurry (down speed ÷ film height) was $3\,s^{-1}$. This shear rate experienced at the printing build plate does not exceed the critical shear rate from slurry rheology flow tests to cause shear-thickening for most slurries in this study; thus, that was why the two slurries pointed out above were printable. The shear rate experienced when the build plate moves into the slurry is critical for retaining the correct rheology of the slurry, and it is thought that this shear event is more dominant and important than the first spreading shear event where the slurries had time to regain the correct shear shinning rheology before getting cured into place at the build plate area.

All slurries from the KD1 coating study were tested for cure depth (Fig. S5). Curing was 5 s at 57 mW/cm^2 power. All slurries from Fig. 6B had cure depths of 40 µm, which means the cure depth was independent of the dispersant amount or order of addition. This cure depth is sufficient for DLP of larger rectangular shapes based on printing layers that are at least half of the cured depth. The slurries C1KD1/4CC42 and C4KD1/1CC42 were both prepared for printing. Directly after mixing these two slurries, they were liquid and flowable. However, the slurry rheology (not actually measured) aged with time after mixing. It was visually observed that these slurries started to become solid within hours after mixing. After approximately 1 day, the slurries would not flow under gravity or under their own weight as shown in Fig. S5. Fortunately, this behavior could be reversed after mixing for 30 s to become a liquid slurry again. This behavior was not foreseen and illustrates how the two dispersants used in tandem are not compatible with the Admatec resin for long time use or longer print times. Further investigation evaluating the impact of this reversible solidification showed that KD1 was the culprit; thus, the use of KD1 was discontinued for printing.

During preliminary printing trials where various light energies were used to stick layers onto the build plate, it was observed that the cured slurry adhered more to the transport film in the printer than to the aluminum build plate. Modifications to the slurries to address the adhesion competition between the transport film and the aluminum build plate were made by adding Disperbyk 103 and glycols to reduce adherence to the transport film[38].

Figure 7A shows shear sweeps of slurry 4CC42 (without the KD1), and the resulting rheological behavior exhibited shear-thickening and instabilities in the $2–11\,s^{-1}$ shear rate range, thus rendering it not as printable as previously stated. By adding 2 wt.% (relative to total slurry) Disperbyk 103 to the slurries with 4 wt.% CC42 (relative to powder), the shear-thickening behavior was reduced, and the slurries adhered less to the transport film. By adding either PG or PEG400 in 1 wt.% (relative to the total slurry composition) to the mixes with Disperbyk 103, the slurries had shear-thinning behavior. All these slurries adhered more to the build plate and less to the transport film. Figure 7B presents the viscosity curves from Fig. 7A along with the corresponding fits based on the power-law fluid model described in Eq. (1). For comparison, the viscosity profile of a commercial Admatec slurry
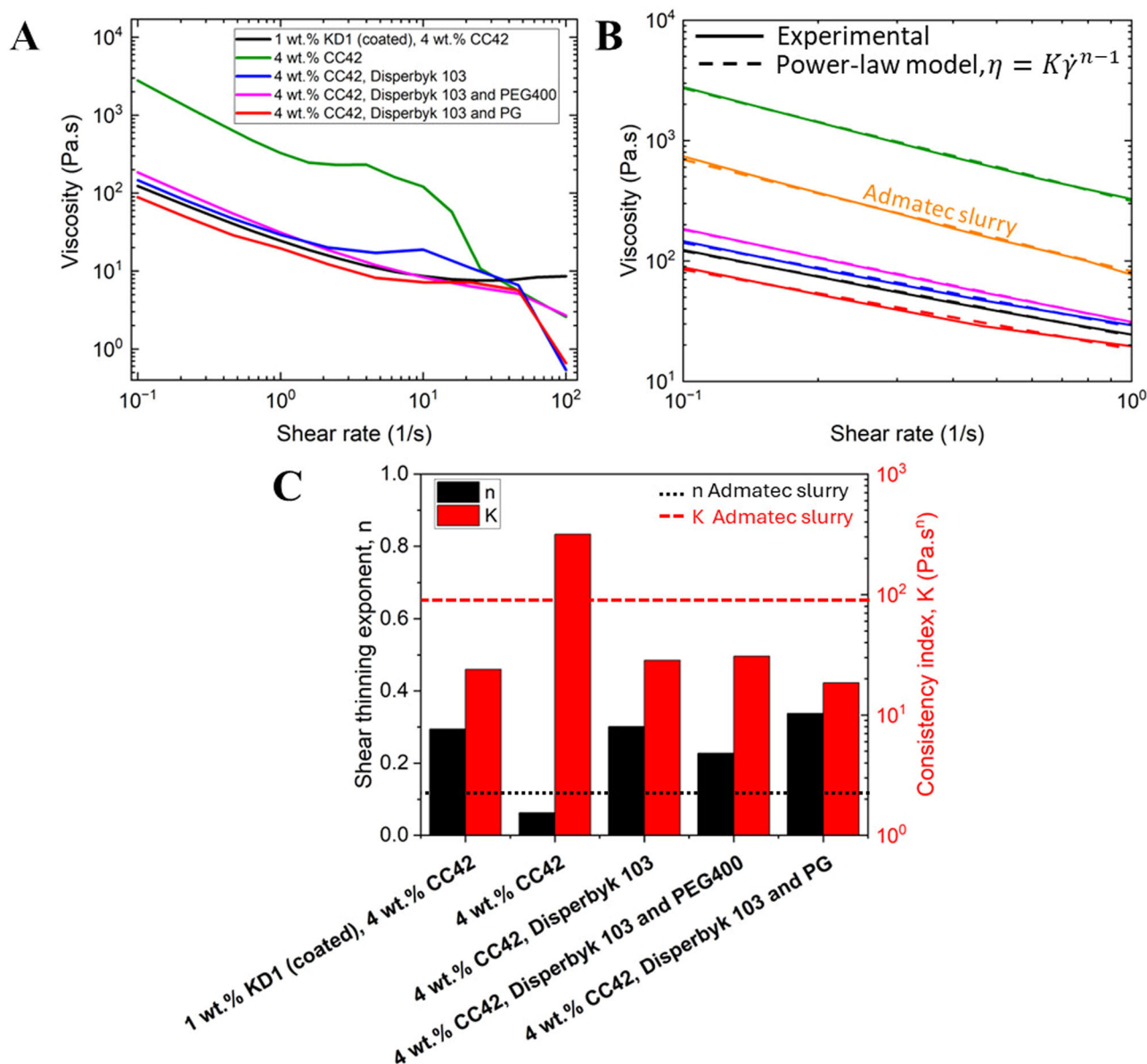
Fig. 7 | Final rheology of the slurries selected for printing. A Log-log plots of viscosity vs shear rate during the rheology flow tests (shear sweeps) for 40 vol.% solids loaded slurries showing the effects of additions to CC42. **B** Log-log plots of viscosity vs. shear rate from (**A**) plotted along with fits to the power-law model described by Eq. (1), applied over the shear rate ranges of 0.1–1 s^{-1}1;. **C** Bar plots of the n and K values computed from the rheology curves by linear regression over the linear portions of the curves in (**B**).

is also included (see Fig. S1). All fits were applied over the linear regions of the curves within the shear rate range of 0.1 to 1 s^{-1}. Figure 7C compares the shear-thinning behavior of the formulated slurries to the commercial Admatec slurry (see Table S1). The dotted and dashed lines represent the values of n and K for the Admatec reference slurry, respectively. While the formulation with 4 wt.% CC42 alone demonstrated favorable shear-thinning ($n = 0.06$), its higher viscosity ($K = 315.7$ Pa·s^n) compared to the commercial slurry may hinder smooth recoating and resin leveling, making it less optimal for VPP applications. Among the other formulated systems, the slurry containing PEG400 showed the most desirable rheological properties for VPP, exhibiting the lowest shear-thinning exponent ($n = 0.22$) and the highest consistency index ($K = 30.8$ Pa·s^n), indicating strong shear-thinning behavior and high low-shear viscosity, respectively. These characteristics are ideal for VPP, as they allow easy flow under shear during recoating while maintaining shape fidelity post-curing. Therefore, PEG400-based slurries were selected for printing due to its combination of flowability under shear and structural retention at rest.

Bars that printed to completion needed more than the amount of energy corresponding to ample cure depth (57 mW/cm^2 (50% powder) corresponding to 40 μm cure depth), which is not typical in oxide ceramic VPP. Printing parameters varied from 50% to 70% power with 5–50 s of cure time. Bend bars were successfully printed as shown in Fig. 8 with 60% power and 30 sec per layer. This excess in energy needed was likely due to the low cure depth of 40 μm and some competition of adherence to the build plate versus the transport film. It could also be due to slurry aging, where photoinitiators lose effectiveness to create free radicals and cure over time. As the debinding process produced no visible cracks in the bend bars, the samples were moved to the sintering stage. The sintering in gas overpressure induced liquid-phase densification from the sintering aids, and the linear shrinkage was 27 ± 2% in the y-direction, 18 ± 3% in the x-direction, and 33 ± 4% in the z-direction. The sintered bend bar is shown in Fig. 8 on the right side of the figure.

Figure 9 shows SEM images of the sintered sample. Figure 9A shows the cross section where long pores or delamination are outlined in green

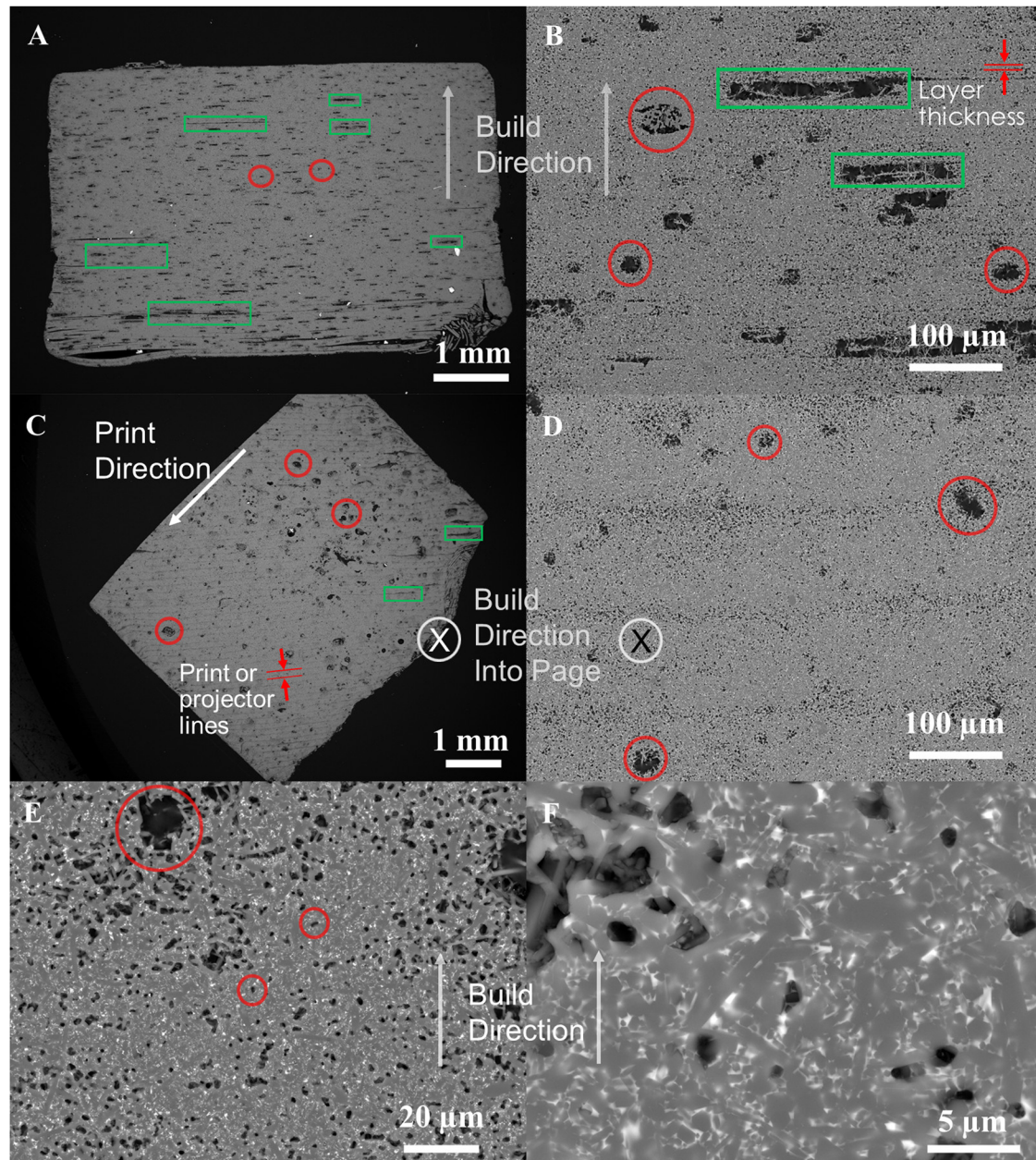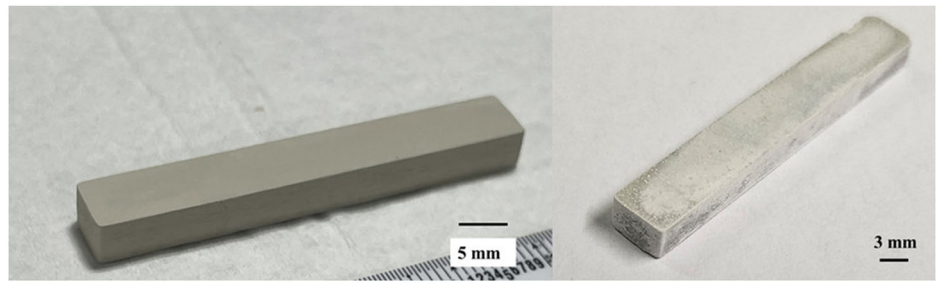**Fig. 8 |** Printed bend bar (left) and sintered bend bar (right).

Fig. 9 | Microstructure of printed and sintered parts. A, **B** Cross sectional, **C**, **D** top view (or through print thickness), and **E**, **F** higher resolution cross sectional SEM images of the microstructure.

rectangles and spherical pores are outlined in red circles. The longer delamination defects that look like long cracks represent 1.61% of the sample from image analysis, and the average length of these delamination defects was 0.75 ± 0.23 mm. These delamination defects were likely due to poor adhesion to the build plate and shear-thickening. Figure 9B shows the shorter elongated defects outlined in green rectangles and areas of spherical defects or voids in red circles. The defects in green rectangles represented 3.27% and are 118 ± 43 μm long 20 ± 13 μm, which means that these are
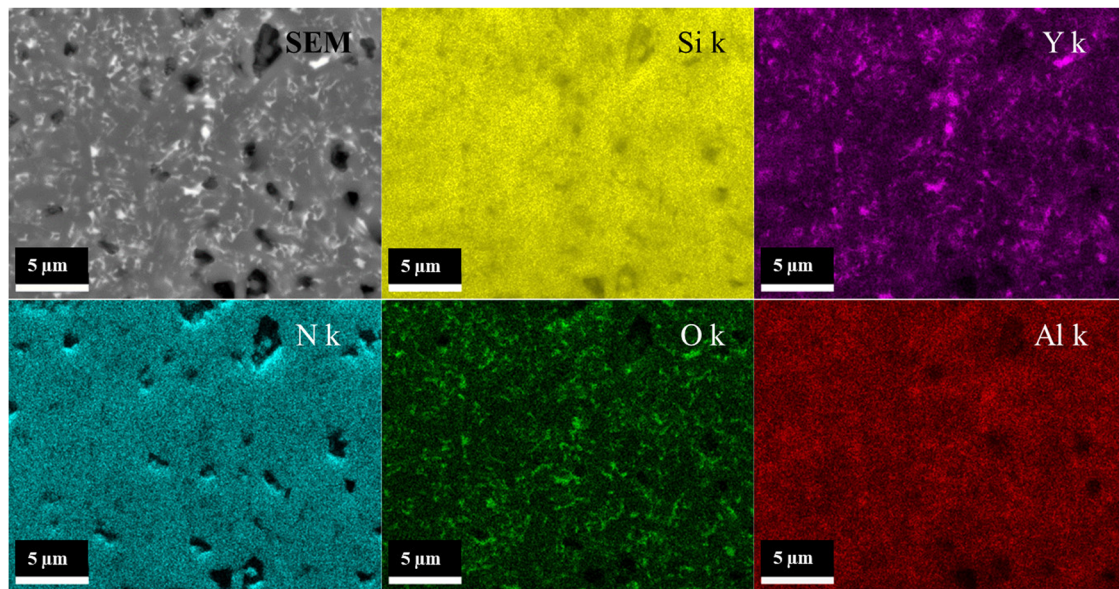
Fig. 10 | SEM/EDS images of the microstructure.

likely areas where 1–3 layers are missing or did not adhere well enough to stick to the next layer. The spherical pore defects in red circles represented 3.85% of the sample and are 24.0 ± 4.5 μm in diameter. These spherical pores may come from poor adhesion and agglomerates in the slurry that cannot be easily broken up with shear mixing or closed with pressure-assisted sintering. The layered pattern pointed out in Fig. 9B shows the spacing is ~8 μm, which is the printing layer thickness after shrinkage. The longer, more striated pores, that are less periodic, may be spreading and peeling flaws that are induced during the printing process. Figure 9C shows the through-thickness direction of the microstructure where the longer pores are outlined in green rectangles and the spherical pores are outlined in red circles. There were less elongated pores observed in the through-thickness direction, and a periodic spacing of about 100 μm was observed. These have been attributed to streak lines or projector lines from the in-plane processing of light. A closer look at the pores and spacing of the smaller pores is shown in Fig. 9D. The larger pores outlined in red circles were close to the same size and amount as the spherical pores in the cross-sectional views. The pores and defects seen in the through thickness direction do not show as many of the long delamination defects as in the cross-sectional images, and that is likely since it is easier to see the peeling and pulling force defects from printing in the cross-sectional views. Figure 9E shows more of the smaller spherical pores which are 9% of the sample at 2.3 ± 1.8 μm, and Fig. 9F shows smaller pores and the microstructures showing the elongated grains. Further investigations were conducted with SEM/EDS and XCT to identify the material in the defects and quantify the pores. From Archimedes measurements, the samples were $85 \pm 4\%$TD dense using a theoretical density of 3.26 g/cc (calculated by rule of mixtures from the addition of sintering aids).

Figure 10 shows the SEM/EDAX images of the cross section of the microstructure. It clearly shows the Si_3N_4 grains surrounded by a grain boundary phase. The Si_3N_4 is not well outlined with the Si-k and N-k maps, but the Si-k signal shows up as slightly less concentrated in the grain boundaries. The N-k is dispersed uniformly throughout the sample. The Y-k, O-K, and Al-k show up very brightly in the grain boundary phase. Clearly the sintering aid has reacted and is residual in the grain boundaries and around Si_3N_4 grains. Some of the larger areas of the oxide show up as strong Y-k signal, so there may have been some agglomerating of the Y_2O_3 powder. There seems to be O, N, Si, Al, and Y in the grain boundary phase, according to EDAX.

Figure 11 shows the XRD patterns of the powders and the printed sample. The Si_3N_4 powders are comprised primarily of alpha phase, the alumina is the corundum alpha phase, and the yttria is alpha phase. The XRD pattern of the sintered sample shows that the majority of the samples is β-Si_3N_4 and small amount of some crystalline $Y_4AlSiNO_8$ phase, which can come from slight crystallization of the Y-Al-Si-N-O glass phase[47]. This was verified by Rietveld analysis with numbers shown in Table 3, where the sintered parts were 92.6 wt.% β-Si_3N_4. Yttrium aluminum garnet (YAG) and Y-Al-Si-N-O can form when in equilibrium with Si_3N_4-Al_2O_3-Y_2O_3, but in the case here, no noticeable amount of YAG was formed.

Figure 12 shows the summary of the XCT results. 3D solid and segmented images of the reconstructed volumes are shown below in Fig. 12A. In Fig. 12A, the red volume shows where larger delamination is located, and the green volume shows where pores and other smaller defect voids are located. There was a larger percentage of smaller pores relative to the delamination defects. A 2D slice from the through printing thickness direction (where the plane is indicated with red arrows in Fig. 12A) is shown in Fig. 12B Here, the defects detected were pores, and inclusions as pointed out with red arrows (this further validates the SEM images from Fig. 9). In Fig. 12C, a 2D slice of the vertical cross section is shown (along the plane indicated with green arrows in Fig. 12A), where the defects detected were smaller pores with some larger delamination cracks as shown with the green arrows. Finally, in Figs. 12D, 2D slices from the horizontal cross section (along the plane indicated with blue arrows in Fig. 12A) are presented. Again, the observed defects consisted mostly of smaller pores, but just like the vertical direction, delamination cracks are visible, indicated with blue arrows. The blue arrows also point to an area on top left corner where the printing layers can be seen, and the volume looks lamellar in structure in that area. That could be from high printing energy from the longer layer cure times needed to get layers to stick to the build plate. The increase in energy can cause extra curing and defects at the print layer interfaces. Likely enough curing occurred to build a part without failing, but the lamellar structure arose from the lack of adhesion and curing into the next layer (likely there are missing layers in those areas as well).

Figure 13 shows the behavior from one mechanical test of an as-printed bend bar in 4-pt flexural tests (all tests showed similar behavior, and the standard deviation is presented in Table 3). The samples load sufficiently, and there is a linear region for the stress increase until the samples exhibit brittle failure. The strength reaches over 300 MPa for the sample size tested.

Figure 14 shows the fracture surface of a tested bend bar as printed where the cross section is roughly 5.6 mm × 3.9 mm. Figure 14B shows the two surfaces of the bend bar where several areas of defects area located as pointed out with red arrows. The neutral axis and the tension side as well as the build direction are pointed out showing that in the orientation tested the tension
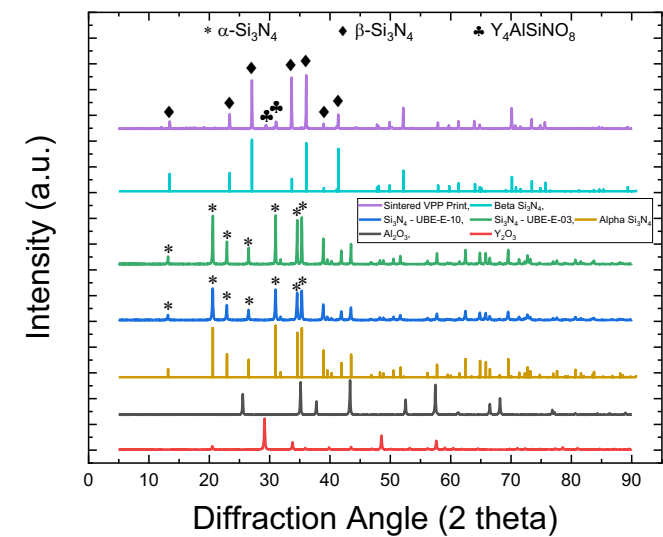
Fig. 11 | XRD patterns of the powders and the printed and sintered materials.

## Table 3 | Density and mechanical testing data of sintered samples.

Density (g/cc)	2.79 ± 0.12
Density (%TD)	85
Strength (MPa)	330 ± 19
Rietveld (wt.%) of powder	E-03: 99.7 (Alpha) E-10: 98.9 (Alpha)
Rietveld (wt.%) of sintered parts	92.6 (β-Si$_3$N$_4$) 7.4 Y$_4$AlSiNO$_8$

side extends down to the side of the sample that was adhered to the build plate, so the failure causing flaws in this orientation of testing are near the start of the printing layers. Figure 14C shows the flaw directly on the surface of the bend bar and one located just inside the volume of the bend bar, and a closer look at these defects shows that they are pores with β-Si$_3$N$_4$ rods that have grown into the pores space. Figure 14A shows another pore that could cause failure, and it also shows that there are β-Si$_3$N$_4$ rods that have grown into the pores space similar to pores that were observed in following[47]. The failure causing flaws seem to be from large pores and not from delamination defects, but more statistical data and fractography would be needed to understand which flaws more commonly cause failure of these parts.

Discussion

The motivation for this work was driven to provide an alternative commercial or off-the-shelf solution for VPP silicon nitride. As shown in this body of work, developing new slurries can be difficult because the dispersion and rheology must be specific to the printing technique chosen. Obtaining the right rheology is critical, and the cure depth must also be sufficient to obtain thick enough layers for printing. Even if those are achieved, it does not guarantee that printing is achievable since adherence to film versus the build plate is an issue with a tape casting-style printer. If noticed in powder supply or slurries, filtering out agglomerates or sieving powder may be needed before mixing. Here, bimodal powder was used to allow more light to penetrate to allow enough cure depth. This study specifically helps the understanding of two common dispersants discussed in literature for Si$_3$N$_4$ VPP, and we introduce other materials that help rheology and create shear-thinning behavior. The dispersant KD1 was not as effective as CC42 and caused solidification, so alternative resins would be needed to use this dispersant effectively. Printing defects can arise from rheological changes like shear-thickening during spreading under the doctor blade as well as when the build plate presses into the slurry, which can also affect the adhesion and defects that arise during printing and adhesion to the build plate. Even with slurry and print defects, relatively low green density, and relatively large primary powder size, silicon nitride parts sintered to closed porosity and

Fig. 12 | X-ray CT of printed and sintered parts. X-ray CT images of a small piece of failed printed bend bar showing **A** the reconstructed 3D volume with pores segmented in green and delamination in red, **B** 2D slice image from the through thickness of the print along the plane indicated with red arrows in (**A**), **C** 2D slice image of the vertical cross section of the print along the plane indicated with green arrows in (**A**), and (**D**) two 2D slice images from the horizontal cross sections of the print obtained along the planes indicated with black arrows in (**A**).
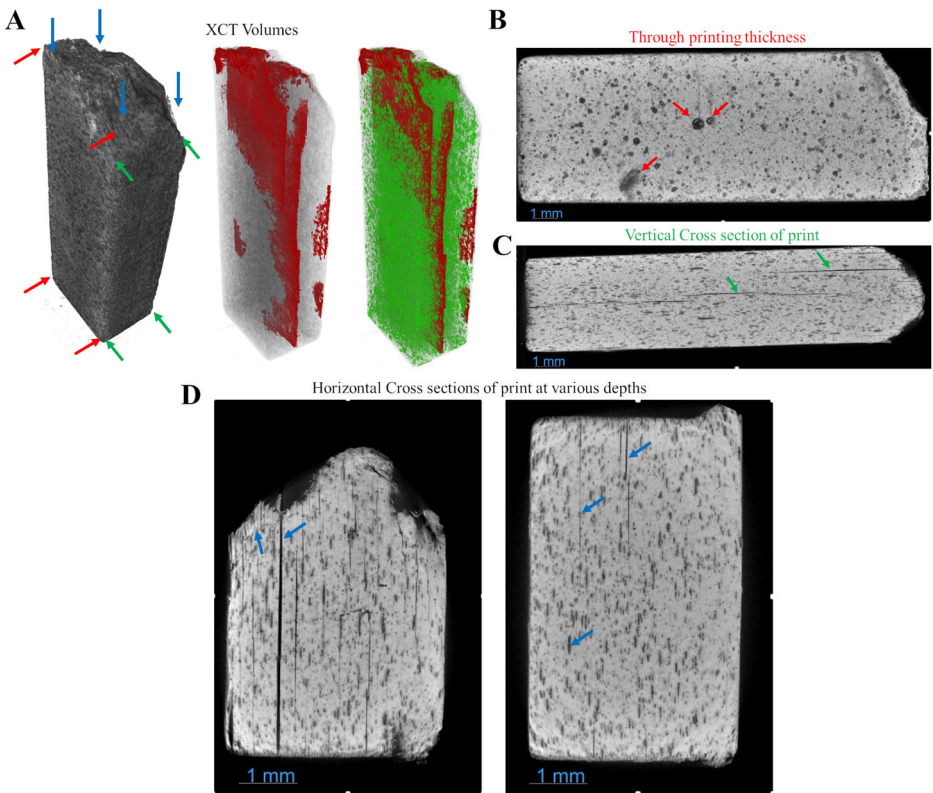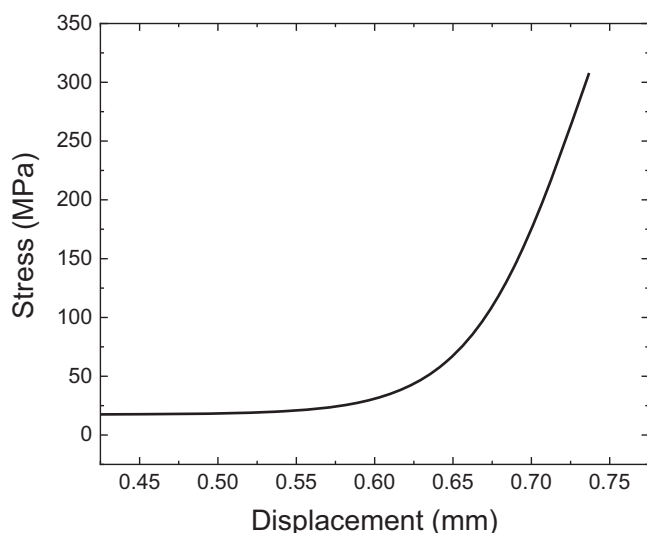
Fig. 13 | Mechanical properties. 4-pt. bend stress-displacement curve.

high density, and display high strength, so this is promising for the future of Si_3N_4 VPP. Stabilization and rheology were measured for slurries utilizing KD1 and CC42 as dispersants. The two dispersant materials had opposite zeta potentials on silicon nitride. The order of mixing showed that CC42 provided rheology stabilization better than KD1, and it can dominate the rheology behavior regardless of when it is added. KD1 grafted and coated onto powder provided all shear-thinning slurries. Slurries with KD1 presented some long-term stability and adhesion issues, so other additives were used to modify rheology and adhesion. Slurries without KD1 were made by adding some other rheological modifier to obtain shear-thinning behavior. The shear-thinning behavior of all formulated slurries was quantified using a power-law fluid model, which enabled comparison against the rheological behavior of a commercial VPP slurry and facilitated the selection of the most suitable formulation for printing. Proper adhesion was achieved with Disperbyk 103 and glycol species. Prints were made with long cure times relative to the standard oxide materials, and some slurry and print defects were detected in the microstructure. Samples were debound and sintered to high density. Pores from agglomerates and large powders were present, but also larger streaks and delamination were present, which could be from peeling and adhesion as well as excess curing need to stick to the build plate. Overall, the microstructure was reflective of liquid-phase sintered Si_3N_4 with slightly crystalline Y-Si-Al-O-N glass in the grain boundaries, density was 85%TD, and the mechanical strength was around 330 MPa.

Methods
Materials
Two grades of silicon nitride were used to make bimodal powder slurries. SN-E03 grade (Ube industries Ltd., Tokyo, Japan) high purity Si_3N_4 powder with a reported D_{50} of 2 μm and a surface area of 2–4 m^2/g was combined in a 70/30 weight ratio with SN-E10 grade (Ube industries Ltd., Tokyo, Japan) high purity Si_3N_4 powder with a reported D_{50} of 0.7 μm and a surface area of 9–13 m^2/g. Alumina (Al_2O_3) and yttria (Y_2O_3) (Stanford Materials) powders with average particle sizes ~400–600 nm were used as the sintering aid powders. The particle size reported by the manufacturers of the Si_3N_4, Al_2O_3, and Y_2O_3 powders was compared to the particle size distribution measured in house by using a Microtrac FlowSync (Model MRB SYNC York, PA, USA) laser diffraction system and dynamic light scattering detector for precision to 0.01 μm. The system performed three consecutive measurements for each sample to ensure repeatability, with results averaged for analysis. The particle size distribution was reported as D10, D50, and D90 values to describe the cumulative size as a function of volume distribution. Brunauer–Emmett–Teller (BET) surface area was done using an ASAP 2020 Plus, Version 2.00 software (Micromeritics, Norcross, GA,
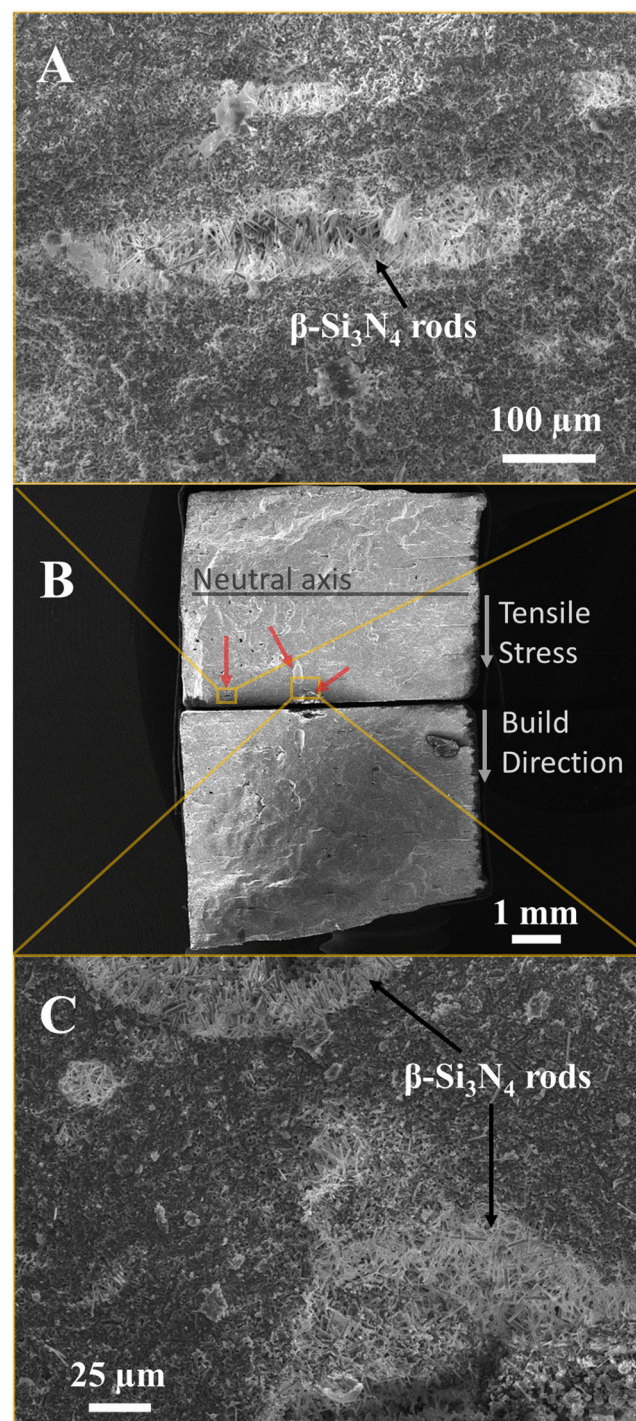

Fig. 14 | Fracture surfaces of tested bend bar showing possible failure and crack initiation. B is the SEM of the entire fracture surface, **A** is a higher magnification SEM image of the spot on the left, and **C** is a higher magnification SEM image of the spot on the right.

USA). Blank C resin (Admatec, Europe) was used as the commercial resin media for mixing of the slurry. Variquat CC 42 NS (polypropoxy quaternary ammonium chloride) and Hypermer Croda KD1 (proprietary, based on polyester/polyamine condensation polymer with a cationic head group) were used as the dispersants. Disperbyk 103 (polyester phosphoric acid ester), polyethylene glycol (PEG) 400, and propylene glycol (PG) were evaluated as rheology modifiers in this study. A commercially available slurry (AdmaPrint A10) was evaluated (Fig. S1) for comparison with the rheological behavior of the slurries formulated in this work.

Article

Slurry making, rheology, and zeta potential

Zeta potential (ζ) was measured on an electrophoresis cell (Zetasizer Pro, Malvern Panalytical, UK) to measure the bare Si_3N_4 powders and various dispersants to evaluate adsorption on single points. Preparation for zeta potential measurements started with making a parent solution by adding 0.08 g silicon nitride to 5 mL of toluene. Toluene was used because it has a known refractive index making it easier to analyze with the zeta potential analyzer directly and measure the dispersants relative to only powder. Dispersants were added to parent solutions in 2 wt.% compared to solids. Aliquots were then made by adding 40 μL of the parent solutions (with and without dispersants) into 20 mL of the solvent (toluene) to achieve a 10-ppm dilution.

Blank resin C was mixed first with dispersants (CC42 or KD), except for when the order of mixing was tested. The order was varied to understand the interactions of the CC42 and KD additives in the slurry constituents. A notation for the various mixes is established to quickly identify the dispersant order and amount, for example slurry 4CC42/1KD1 is a slurry in which the order of mixing is as follows: resin, 4 wt.% CC42, E-03, E-10, KD1 in 1 wt.%, yttria, alumina. Commonly, dispersants are added to the solvent before the powder so that the dispersants can be intimately mixed and provide uniform adsorption onto the powder before other additives can compete with the adsorption. Binder, plasticizer, or lubricant was added after powder addition to determine if they interact with the dispersant and subsequently bind to the polymer once dried or cured. Thus, the order of addition was tested by adding CC42 or KD components before and after powder addition. To mix a slurry, the blank resin C was first mixed with the dispersant (CC42 or KD depending on the test) then SN-E03 powder, SN-E10, yttria powder, alumina powder, dispersants (CC42 or KD depending on the test) were added in that order. After each additional material was added, the slurry was mixed for 15 s at 1200 rpm in a Thinky Mixer (Thinky ARV-310LED, Laguna Hills, CA). Once the final constituents were added, the resulting slurry was mixed for 1 min at 1200 rpm in the Thinky mixer. To improve rheology by lowering the viscosity while keeping the slurries shear-thinning in a large range of shear rates, Disperbyk 103 and either PEG400 or PG were added subsequently and mixed additionally the same way. All slurry formulations and their abbreviations are shown in Table 4.

Rheology flow tests were run with aluminum parallel plates with a 1 mm operating gap on a strain-controlled rheometer (ARES G2, TA Instruments, New Castle, DE) to measure viscosity as a function of shear rate. Shear ramps were used to screen slurries for shear-thickening behavior by continuously ramping the shear rate from 0.1 to 100 s^{-1} in 2 min. Logarithmic shear sweeps were performed using a 5 min pre-shear at 1 s^{-1} followed by a shear sweep from 0.1 to 100 s^{-1}. During the sweep, each shear rate was allowed to equilibrate for 5 min before averaging data over 4 s to record a measurement.

Slurry rheological modeling

The shear-thinning behavior of complex fluids is commonly characterized using the power-law model, which relates viscosity (η) to shear rate ($\dot{\gamma}$) through the following expression[48–50]:

$$\eta = K\dot{\gamma}^{n-1} \tag{1}$$

In this equation, two key parameters define the flow characteristics of the fluid, or slurry in this case: the consistency index (K) and the shear-thinning exponent or flow index (n). The consistency index, K, is a measure of the fluid's viscosity magnitude and reflects the apparent viscosity at a reference shear rate of 1 s^{-1}1;. It carries units of Pa·s^n and can be thought of as an indicator of the fluid's overall resistance to flow. Higher values of K correspond to thicker or more viscous fluids under low shear conditions, while lower K values indicate thinner or more easily flowing fluids. In practical terms, K is influenced by factors such as particle concentration, molecular weight, temperature, and the presence of dispersants in the system. The second parameter, the flow index (n), describes how the viscosity changes with increasing shear rate: $n < 1$ denotes *shear-thinning*

Table 4 | Slurry identification table for order of mixing in relation to both silicon nitride powders

Slurry ID	Wt.% KD1, order added	Wt.% CC42, order added
1KD1/1CC42	1, before powder	1, after powder
1KD1/2CC42	1, before powder	2, after powder
1KD1/4CC42	1, before powder	4, after powder
2KD1/1CC42	2, before powder	1, after powder
4KD1/1CC42	4, before powder	1, after powder
1CC42/1KD1	1, after powder	1, before powder
1CC42/2KD1	2, after powder	1, before powder
1CC42/4KD1	4, after powder	1, before powder
2CC42/1KD1	1, after powder	2, before powder
4CC42/1KD1	1, after powder	4, before powder
C1KD1/1CC42	1, coated onto powder	1, after powder
C1KD1/2CC42	1, coated onto powder	2, after powder
C1KD1/4CC42	1, coated onto powder	4, after powder
C2KD1/1CC42	2, coated onto powder	1, after powder
C4KD1/1CC42	4, coated onto powder	1, after powder
4CC42	--	4, before powder
4CC42/2BYK103	--	4, before powder
4CC42/2BYK103/ 1PEG400	--	4, before powder
4CC42/2BYK103/1PG	--	4, before powder

Slurries with Disperbyk 103, PG, and PEG400 all had those constituents added after the entire slurry was made to modify the rheology.

(pseudoplastic) behavior, where viscosity decreases with shear rate; $n = 1$ indicates *Newtonian* behavior, where viscosity remains constant; $n > 1$ corresponds to *shear-thickening* (dilatant) behavior, where viscosity increases with shear rate. On a log-log plot of viscosity versus shear rate, the slope of the linear portion of the curve is equal to $1 - n$. Numerical values for n and K were computed from the viscosity vs. shear rate curves by linear regression over the linear portions of the curves (see Table S1 and Table S2).

Cure tests, printing, and cleaning

The depth of cure tests were performed by spreading slurry onto the transport film and irradiating the slurry in a checkerboard pattern with a known energy level for a fixed amount of time. Then the uncured slurry was cleaned from the transport film with Kimwipe, leaving only the cured polymer on the film. The cured layer of Si_3N_4 was measured while on the transport film with calipers, and cure depth of 2x the desired print layer is typically used to provide intimate contact with the underlying layer. Most of the depth of cure tests were performed with 5 s of cure time at 50% power (57 mW/cm^2), which are typical conditions for ceramic VPP. An Admaflex 130 (ADMATEC Europe BV, The Netherlands) printer was used to print bend bars of 50 mm (y-direction, normal to the foil transport direction) × 7 mm (x-direction, parallel to foil transport direction) x 5 mm (z-direction, through thickness or build direction) with varying light intensity (50–70%) and curing times (5–50 s). The doctor blade gap height was 70 μm, and the printing layer thickness was 10 μm. The transport foil speed was 40 mm/s (and the slurry transports 10 cm from doctor blade to printing area), and the peeling up speed of the build plate was 200 μm/s during peeling and 6 mm/s after peeling of build from the transport foil. The speed of the build plate down into the slurry was 6 mm/s until it was 1 mm away from the slurry, and then it was 200 μm/s as the build plate physically contacted the spread material and pushed down into the slurry. The build plate moves up 6 mm after each layer. There was a 10 s delay before printing each layer. After printing, removal of uncured slurry from the printed parts was performed by soaking in a water bath for 24 h.

Article

Binder burnout and sintering

Printed bend bars were debound in an air furnace using the same heating as in our previous work[29]. After debinding, the bars were subsequently sintered in a graphite furnace with gas overpressure or gas pressure sintering (GPS). Samples were heated to 1010 °C under vacuum, then N_2 was flown at 1 L/min during ramping to 1200 °C at 1.67 °C/min, ramping temperature again to 1700 °C at 5 C/min, and yet again, ramping from 1700 to 1820 °C at 2 °C/min. During the 1700 to 1820 °C ramp, the N_2 pressure was increased from atmospheric to 10 MPa, and both temperature and pressure were held for 1 h. After the hold, the bend bars were cooled at 2.67 °C/min, and atmospheric N_2 pressure was reached by bleeding the system in 10 min.

Characterization and mechanical properties

X-ray diffraction (XRD) was performed with continuous θ-2θ scans on the Panalytical X'pert PRO diffractometer from nominally 5 to 90° 2θ using CuKα radiation (λ = 1.540598 Å). All scans used 1/4° fixed slits, 1/2° anti-scatter slit, 0.04 Soller slits coupled with a 10 mm mask (beam length). For the phase identification procedure, a search match was conducted using the Jade 2010 software and the ICDD PDF-4 (2022) database.

X-ray computed tomography (XCT) measurements were performed using a Zeiss Xradia Versa 520 instrument to help identify delamination, pores, defects, and distortion. The scans utilized 100 kV x-rays at a total 9 W power. A 4x scintillator objective was used together with geometric magnification. Coupled with a 1×1 binning on the detector, a 3.73 μm voxel size was achieved. The data analysis and visualization were performed with a Dragonfly PRO v.2022.2 software.

The scanning electron microscopy (SEM) was done in a TESCAN MIRA3 XMH Schottky FE-SEM with the EDAX Octane Elect Super Silicon Drift Detector. SEM images were collected at 20 kv, 14 mA, and a spot size of 15 nm. SEM of the powders was achieved by adhering the powders to carbon tape with known volume for all samples. The energy-dispersive X-ray analysis (EDAX) was done at 20 kv, 18 mA, and spot size of 75 nm. Both the SEM and EDAX were done secondary electron mode.

Four-point bending tests were performed on 5 bend bars as processed through the sintering steps with dimensions of roughly ~39 mm (y-direction) x ~ 6 mm (x-direction) x ~ 4 mm (z-direction) to measure the flexural strength following the procedure outlined in ASTM C1161 using an electromechanical test frame (Instru-Met, 1210AF-300-B) and a silicon carbide fixture. The crosshead speed was 0.001 inch/s.

Data availability

Available upon request and DOE approval.

References

1. Dong, X. et al. Additive manufacturing of silicon nitride ceramics: a review of advances and perspectives. *Int. J. Appl. Ceram. Technol.* **19**, 2929–2949 (2022).
2. Wiederhorn, S. M. & Ferber, M. K. Silicon nitride for gas turbines. *Curr. Opin. Solid State Mater. Sci.* **5**, 311–316 (2001).
3. Yoshida, M., Tsuruzono, S., Ono, T., & Gejima, H., "Development of Silicon Nitride Rotors for Gas Turbine Applications," *Proc. ASME Turbo Expo*. (2015).
4. I. E. Systems, "DoE Advanced Ceramic Microturbine," (2004).
5. Ustundag, E., & Fischmannn, G., "Cost modeling and analysis for advanced structural silicon nitride turbomachinery ceramics," pp. 208–216 (2008).
6. Vikulin, V. Production of Si3N4-based articles and their application in aerospace industry. *Adv. Sci. Technol.* **45** (2006).
7. R. H.- Ceramics and undefined 2021, "Silicon nitride, a close to ideal ceramic material for medical application," *mdpi.comRB HeimannCeramics, 2021•mdpi.com*.
8. Zhao, S. et al. Robocasting of silicon nitride with controllable shape and architecture for biomedical applications. *Int. J. Appl. Ceram. Technol.* **14**, 117–127 (2017).
9. R. Zhang, D. Fang, X. Chen, Y. P.-C. International, and undefined 2012, "Effect of pre-oxidation on the microstructure, mechanical and dielectric properties of highly porous silicon nitride ceramics. (Elsevier, 2012).
10. Bocanegra-Bernal, M. H. & Matovic, B. Dense and near-net-shape fabrication of Si3N4 ceramics. *Mater. Sci. Eng. A* **500**, 130–149 (2009).
11. Yang, X. et al. Fabrication and properties of porous silicon nitride wave-transparent ceramics via gel-casting and pressureless sintering. *Mater. Sci. Eng. A* **663**, 174–180 (2016).
12. Penas, O., Zenati, R., Dubois, J., G. F.-C. International, and undefined 2001, "Processing, microstructure, mechanical properties of Si3N4 obtained by slip casting and pressureless sintering. *Ceramics International*. (Elsevier, 2001).
13. Bitterlich, B. & Heinrich, J. G. Aqueous tape casting of silicon nitride. *J. Eur. Ceram. Soc.* **22**, 2427–2434 (2002).
14. Zocca, A., Colombo, P., Gomes, C. M. & Günster, J. "Additive manufacturing of ceramics: issues, potentialities, and opportunities,". *J. Am. Ceram. Soc.* **98**, 1983–2001 (2015).
15. Chen, Z. et al. 3D printing of ceramics: a review. *J. Eur. Ceram. Soc.* **39**, 661–687 (2019).
16. Cramer, C. L. et al. Additive manufacturing of ceramic materials for energy applications: Road map and opportunities. *J. Eur. Ceram. Soc.* **42**, 3049–3088 (2022).
17. Aguirre, T. G., Cramer, C. L. & Mitchell, D. J. Review of additive manufacturing and densification techniques for the net- and near net-shaping of geometrically complex silicon nitride components. *J. Eur. Ceram. Soc.* **42**, 735–743 (2022).
18. Rabinskii, L. N., Ripetskii, A. V., Pogodin, V. A., Sitnikov, S. A. & Solyaev, Y. O. Study of porous ceramic based on silicon nitride prepared using three-dimensional printing technology. *Refract. Ind. Ceram.* **57**, 600–604 (2017).
19. Cappi, B., Özkol, E., Ebert, J. & Telle, R. Direct inkjet printing of Si3N4: Characterization of ink, green bodies and microstructure. *J. Eur. Ceram. Soc.* **28**, 2625–2628 (2008).
20. Yu, S. et al. Fabrication of Si3N4–SiC/SiO2 composites using 3D printing and infiltration processing. *Ceram. Int.* **47**, 28218–28225 (2021).
21. Rangarajan, S., Qi, G., Venkataraman, N., Safari, A. & Danforth, S. C. Powder processing, rheology, and mechanical properties of feedstock for fused deposition of Si3N4 ceramics. *J. Am. Ceram. Soc.* **83**, 1663–1669 (2004).
22. He, G. P., Hirschfeld, D. A., Cesarano, J. III & Stuecker, J. N. Robocasting and mechanical testing of aqueous silicon nitride slurries. No. SAND2000-1493C. Sandia National Lab.(SNL-NM), Albuquerque, NM (United States); Sandia National Lab.(SNL-CA), Livermore, CA (United States, 2000).
23. Jiang, Q. et al. Fabrication and properties of Si2N2O-Si3N4 ceramics via direct ink writing and low-temperature sintering. *Ceram. Int.* **48**, 32–41 (2022).
24. Costakis, W. J. et al. Material extrusion of highly-loaded silicon nitride aqueous inks for solid infilled structures. *Add. Manuf.* **64**, 103425 (2023).
25. Rueschhoff, L. M., Youngblood, J. P. & Trice, R. W. Stabilizing Highly Loaded Silicon Nitride Aqueous Suspensions Using Comb Polymer Concrete Superplasticizers. *J. Am. Ceram. Soc.* **99**, 3857–3865 (2016). no. 12.
26. Birmingham, B. R. & Marcus, H. L. Solid freeform fabrication of silicon nitride shapes by selective laser reaction sintering (SLRS). In SFF Symposium. Texas. 1995.
27. Wei, Z.-H. et al. Direct fabrication mechanism of pre-sintered Si3N4 ceramic with ultra-high porosity by laser additive manufacturing. *Scr. Mater.* **173**, 91–95 (2019).
28. Wang, K. et al. Preparation of high-strength Si3N4 antenna window using selective laser sintering. *Ceram. Int.* **48**, 2903–2911 (2022). no. 2.

29. Cramer, C. L. et al. Accuracy of stereolithography printed alumina with digital light processing. *Open Ceram.* **8**, 100194 (2021).

30. Cramer, C. L., Raftery, A. M. & Nelson, A. T. Lithography-based Ceramics Manufacturing Technologies. No. ORNL/TM-2019/1365. Oak Ridge National Laboratory (ORNL), Oak Ridge, TN (United States, 2019).

31. Altun, A. A., Prochaska, T., Konegger, T. & Schwentenwein, M. Dense, strong, and precise silicon nitride-based ceramic parts by lithography-based ceramic manufacturing. *Appl. Sci.* **10**, 996 (2020).

32. Wu, X., Xu, C. & Zhang, Z. Development and analysis of a high refractive index liquid phase Si 3 N 4 slurry for mask stereolithography. *Ceram. Int.* **48**, 120–129 (2022).

33. Huang, R. J. et al. Fabrication of complex shaped ceramic parts with surface-oxidized Si3N4 powder via digital light processing based stereolithography method. *Ceram. Int.* **45**, 5158–5162 (2019).

34. Zhan. L., Xia, Y., Zhang, X., Liu, Y., Liu, S. *Effects of Stereolithography Process Parameters on the Curing Properties of Si3N4 Ceramic Slurries*. (Elsevier, 2023).

35. Schwarzer-Fischer, E. et al. CerAMfacturing of silicon nitride by using lithography-based ceramic vat photopolymerization (CerAM VPP). *J. Eur. Ceram. Soc.* **43**, 321–331 (2023).

36. Wang, L., Wang, L., Hao, Z., Tang, W. & Dou, R. Microstructure and properties of silicon nitride ceramics fabricated by vat photopolymerization in combination with pressureless sintering. *Ceram. Int.* **50**, 10485–10496 (2023).

37. Chen, Z. et al. Fabrication of broadband wave-transparent Si3N4 ceramics with octet-truss lattice structure by vat photopolymerization 3D printing technology. *J. Eur. Ceram. Soc.* **44**, 2026–2036 (2024).

38. Li, X. et al. Rheology and curability characterization of photosensitive slurries for 3D printing of Si3N4 ceramics. *Appl. Sci.* **10**, 6438 (2020).

39. Liu, Y. et al. Formation mechanism of stereolithography of Si3N4 slurry using silane coupling agent as modifier and dispersant. *Ceram. Int.* **46**, 14583–14590 (2020).

40. Liu, Y. et al. Stereolithographical fabrication of dense Si3N4 ceramics by slurry optimization and pressure sintering. *Ceram. Int.* **46**, 2063–2071 (2020).

41. Yang, P. et al. Digital light processing 3D printing of surface-oxidized Si3N4 coated by silane coupling agent. *J. Asian Ceram. Soc.* **10**, 69–82 (2022).

42. Zou, W., Yang, P., Lin, L., Li, Y. & Wu, S. Improving cure performance of Si3N4 suspension with a high refractive index resin for stereolithography-based additive manufacturing. *Ceram. Int.* **48**, 12569–12577 (2022).

43. Wu, X., Xu, C. & Zhang, Z. Preparation and optimization of Si3N4 ceramic slurry for low-cost LCD mask stereolithography. *Ceram. Int.* **47**, 9400–9408 (2021).

44. Bove, A., Calignano, F., Galati, M. & Iuliano, L. Photopolymerization of ceramic resins by stereolithography process: a review. *Appl. Sci.* **12**, 3591 (2022).

45. I. de Camargo, M. Morais… C. F.-C. *A review on the rheological behavior and formulations of ceramic suspensions for vat photopolymerization*. (Elsevier, 2021).

46. Lin, L. et al. *Additive manufacturing of complex-shaped and high-performance aluminum nitride-based components for thermal management*. (Elsevier, 2022).

47. Boley, B. A. et al. Sintering of Si3N4-Y2O3-Al2O3. vol. 63, no. 4, pp. 21–1033, (Wiley, 1947).

48. Hmeidat, N. S. et al. Mechanical anisotropy in polymer composites produced by material extrusion additive manufacturing. *Addit. Manuf.* **34**, 101385 (2020).

49. Hmeidat, N. S., Kemp, J. W. & Compton, B. G. High-strength epoxy nanocomposites for 3D printing. *Compos. Sci. Technol.* **160**, 9–20 (2018).

50. Kemp, J. W., Hmeidat, N. S. & Compton, B. G. Boron nitride-reinforced polysilazane-derived ceramic composites via direct-ink writing. *J. Am. Ceram. Soc.* **103**, 4043–4050 (2020).

Author contributions

C.C. designed experiments, made samples, analyzed samples and data, and wrote the paper. P.S. performed data generation and analysis, and manuscript editing. E.C. performed the XRD and XCT measurements and data analyses and reviewed the manuscript. S.B. performed studies on the UV curative system, dispersion additives, and data analysis. T.A. performed data analysis, editing, and discussion. M.M. performed sample characterization and analysis and manuscript editing. B.A. assisted in experimental design, analysis of results, manuscript writing, discussion, and editing.

Competing interests

The authors declare no competing interests.

Additional information

Supplementary information The online version contains supplementary material available at https://doi.org/10.1038/s44334-025-00051-y.

Correspondence and requests for materials should be addressed to Corson L. Cramer.

Reprints and permissions information is available at http://www.nature.com/reprints

Publisher's note Springer Nature remains neutral with regard to jurisdictional claims in published maps and institutional affiliations.